Journal of Marine Science and Technology, Vol. 24, No. 6, pp. 1194-1203 (2016)
DOI: 10.6119/JMST-016-1026-8

PRELIMINARY STUDY OF INTERNAL SOLITARY WAVE AMPLITUDE OFF THE EAST COAST OF KOREA BASED ON SYNTHETIC APERTURE RADAR DATA

Dan-Bee Hong[1], Chan-Su Yang[1,2,3], and Kazuo Ouchi[4]

Key words: synthetic aperture radar, internal solitary wave amplitude, varying surface currents, small perturbation method, Korteweg-deVries equation, action balance equation.

ABSTRACT

This paper presents a method of retrieving the amplitude of oceanic internal solitary wave (ISW), from synthetic aperture radar (SAR) data, and preliminary results obtained in the East/Japan Sea off the east coast of Korean Peninsula. The retrieval algorithms include the small perturbation method (SPM) for microwave backscatter, the action balance equation (ABE) for describing the interaction between wind-generated ocean waves and varying surface current, and also the Korteweg-deVries (KdV) (non-linear partial differential) equation for describing the surface current variation induced by an internal soliton. The radar cross section (RCS) was computed, and the ISW amplitude was estimated by fitting the RCS ratio to the SAR image of ISWs acquired by RADARSAT-1 through the ABE and KdV. Assuming that ISWs propagate along an isotherm between 5°C and 10°C as a boundary between upper and lower layers, ISW amplitude was estimated in the range of 12.5 m~52.5 m. Although no *in-situ* data are available to validate the results, this study is the first of its kind to obtain the underwater information by SAR in the east coast of Korea.

I. INTRODUCTION

Satellite remote sensing has been widely used to measure the physical properties of ocean because of its wide and repeated coverage. Among many satellite sensors, synthetic aperture radar (SAR) is considered as one of the most effective sensors for its all-weather and day-and-night data acquisition capability (Moreira et al., 2013). The penetration depth of microwave into sea water is a few millimeters or less, and therefore SAR does not directly image underwater phenomena. However, underwater phenomena such as internal waves (IWs) are often observed by SAR through the difference in sea surface roughness induced by the hydrodynamic interaction between the wind waves and varying surface current, and the surface current variation in turn is caused by underwater dynamics (Alpers and Hennings, 1984; Lyzenga et al., 2004). While direct measurement of IW properties by thermistor chains and current meters is accurate with limited spatial coverage, measurement by SAR remote sensing is able to provide a wide coverage (order of tens to several hundred kilometers) of IWs.

The oceanic IWs are produced in the interior of the ocean and propagate along a pycnocline (Jackson, 2004; Li et al., 2011; Jackson et al., 2012). The oceanic IWs are generated, in general, by the interaction between the bottom topography with tidal currents (Nycander, 2005), and retain their shape (known as a solitary wave or soliton) for a long period of time. The internal solitary waves (ISWs or solitons) are a particular type of IWs and they appear often in nature as an isolated wave or packets of oscillations with several cycles varying from a few to a few dozens. The wave packets show the dominant features including non-sinusoidal oscillations, nonlinear, mainly downward displacements, and rank-ordered amplitude, wavelength and crest length, and also they appear as quasi-linear stripes in satellite image (Apel, 2002). IWs are one of the important underwater phenomena because of their strong impact on the energy transport (Apel, 2002; Alford, 2003; Nycander, 2005; Pomar et al., 2012; Muacho et al., 2013), nutrient mixing, sediment resuspension, sonar systems, and also underwater communication (Zhou and Zhang, 1991; Hyder et al., 2005).

The generation and propagation properties of IWs in the East/Japan Sea have been studied by several researchers. There are two types of IWs generated by different mechanisms. The first type is the wind-induced near-inertial IW. In May 1999, Kim

Paper submitted 05/27/16; revised 10/06/16; accepted 11/10/16. Author for correspondence: Chan-Su Yang (e-mail: yangcs@kiost.ac.kr).
[1] Marine Safety Research Center, Korea Institute of Ocean Science and Technology, Korea.
[2] Department of Convergence Study on the Ocean Science and Technology, Ocean Science and Technology School, Korea.
[3] Integrated Ocean Sciences, Korea University of Science and Technology, Korea.
[4] Space Development Department, IHI Corporation, Japan.

et al. (2001) measured several packets of IWs off the east coast of Korea with the water depth of 100 m~120 m using Acoustic Doppler Current Profiler (ADCP). They found that the IWs had a time period of 19 hours and this period is close to the local inertial frequency rather than the tidal period, and the maximum displacement of solitary IW reached about 21 m. Kim et al. (2005) reproduced the IWs using a linear model, showing that the waves observed off the East Coast of Korea between April 25 and June 27 were driven by the local wind stress. Kim et al. (2005) observed the IWs generated by wind-induced near-inertial waves in the mid-western part of the East/Japan Sea in May 2004 using an ENVISAT ASAR image. The second type of IWs is associated with the internal tide. Lie et al. (1992) observed the semi-diurnal internal tides with the amplitude of 10 m in the water depth of 50 m using a thermistor chain in summer of 1980 off Jukbyun on the mid-east coast of Korea. From June 1999 to July 2001, an experiment of continuous acoustic travel-time measurement was conducted using an array of 23 pressure-sensor-equipped inverted echo sounders (PIES) and semidiurnal internal tides were observed. From this experiment, Park and Watts (2006) observed the internal tide with a vertical displacement of the 5°C isotherm reaching up to 25 m around 35.8°N and 130.5°E. Note that the IW amplitude can be approximately estimated as the half of the vertical displacement. Park and Watts (2006) also found that a warm (and cold) eddy affects the path of internal tide propagation as demonstrated using a SAR image taken in September 1996 by Nam and Park (2008). In September 2012, Jeon et al. (2014) observed internal tides at a continental shelf-slope region around the northern entrance of the Korea Strait (35.62°N, 130.03°E), and the maximum displacement of 5°C isotherm was 70 m. From the previous studies, the varied amplitudes of IW were observed, and they inferred that the maximum amplitude of IWs was observed near a continental shelf-slope region and it decreased as getting away from that region. Among others, understanding of IWs in the East/Japan Sea is an important issue, but to interpret ISWs using microwave scattering models and SAR images, further studies are required.

In this study, preliminary results are presented on the estimation of ISW amplitude from a SAR image using the small perturbation method (SPM) for modeling radar backscatter (Rice, 1951; Wright, 1968; Ulaby et al., 1982; Yang et al., 2010; Demir et al., 2012), the action balance equation (ABE) to describe the waveheight spectrum perturbed by varying surface currents (Hughes, 1978; Lamy et al., 2004; Ding and Wang 2011), and the Korteweg-deVries (KdV) equation to relate the IW dynamics to the near-surface currents (Korteweg and de Vries, 1895; Osborne and Burch, 1980; Zheng et al., 2001; Chen et al., 2011). First, the parameters entering the solution, i.e., a form of soliton, of the KdV equation including the water densities and water depths are obtained from external sources, and the surface current velocity induced by the ISW is computed. The radar cross section (RCS) from the sea surface in the presence of the varying current is then computed using the Phillips spectrum and the SPM. Finally, the computed RCS is compared with the SAR image of ISW acquired by RADARSAT-1 in the east coast of Korean Peninsula. The amplitudes of ISW are computed by fitting the RCS ratio computed by the SPM to the SAR image of ISW.

This paper is organized as follows. In section 2, the basic theory is described including the SPM, the waveheight spectrum perturbed by a varying surface current using the ABE and the internal soliton based on the KdV equation. In section 3, the experimental site, SAR data, and method to estimated ISW amplitude are presented. In section 4, results with discussions are presented followed by conclusions.

II. COMPUTATION OF THE SAR IMAGE MODULATION

1. Small Perturbation Method

Apart from manmade objects above sea surface and sea sprays associated with whitecaps, the dominant radar backscatter from the sea surface is surface scattering, and several scattering theories have been proposed (Valenzuela, 1968; Ulaby et al., 1982). Among these models, a simplest method is the Bragg-based SPM (Rice, 1951; Wright, 1968) in which the scattering surface is assumed to be slightly rough in comparison with the radar wavelength and the local slope is small compared with local radii of surface curvature. The backscatter RCS based on the SPM is defined as

$$\sigma_{mn}(\theta_i) = 8\pi k_r^4 \cos^4\theta_i \left| g_{mn}^{SPM}(\theta_i) \right|^2 \left(\psi(k_B) + \psi(-k_B) \right), \quad (1)$$

where σ_{mn} $(m, n \in \{H, V\})$ is the RCS of mn polarization, θ_i is the incidence angle, $k_r = 2\pi/\lambda$ is the radar wave-number, λ is the wavelength, $k_B = 2k_r \sin\theta_i$ is the Bragg wavenumber, ψ is the wavegheight spectrum, and g_{mn}^{SPM} is the Fresnel reflection coefficient defined by

$$g_{HH}^{SPM}(\theta_i) = \frac{\epsilon_r - 1}{\left(\cos\theta_i + \left(\epsilon_r - \sin^2\theta_i \right)^{\frac{1}{2}} \right)^2},$$
$$g_{VV}^{SPM}(\theta_i) = \frac{\left(\epsilon_r - 1 \right)\left(\epsilon_r \left(1 + \sin^2\theta_i \right) - \sin^2\theta_i \right)}{\left(\epsilon_r \cos\theta_i + \left(\epsilon_r - \sin^2\theta_i \right)^{\frac{1}{2}} \right)^2}, \quad (2)$$

where ϵ_r is the complex permittivity of the sea water. For the sea water of salinity 35 psu at 20°C, it is given by $\epsilon_r = 65 - 36i$ for C-band microwave (Klein and Swift, 1977). Thus, in the SPM, the principal scatterers are the small-scale ocean waves that satisfy the Bragg resonance condition, and the backscatter RCS can be computed once the waveheight spectrum perturbed by varying surface currents is known.

2. Perturbed Waveheight Spectrum

In the presence of spatially and temporally varying currents induced by ISWs, the ambient waveheight spectrum is perturbed, and their hydrodynamic interaction can be described by the ABE (Hughes, 1978)

$$\left(\frac{\partial}{\partial t}+\frac{\partial\omega}{\partial\mathbf{k}}\frac{\partial}{\partial\mathbf{r}}-\frac{\partial\omega}{\partial\mathbf{r}}\frac{\partial}{\partial\mathbf{k}}\right)N(\mathbf{k};\mathbf{r},t)=S(\mathbf{k};\mathbf{r},t), \tag{3}$$

where $\mathbf{k}$ is the wave number vector of ocean surface waves, $\mathbf{r}$ is the position vector, and t is the time variable. In this ABE, $N(\mathbf{k};\mathbf{r},t)$ is the action spectrum and $S(\mathbf{k};\mathbf{r},t)$ is the source function which describes wave growth and dissipation. $\omega(\mathbf{k};\mathbf{r},t)$ is the apparent wave angular frequency as measured in a frame moving with the current field $\mathbf{U}(\mathbf{r},t)$, which is given by $\omega(\mathbf{k};\mathbf{r},t)=\omega_0(k)+\mathbf{k}\cdot\mathbf{U}(\mathbf{r},t)$, where ω_0 is the intrinsic frequency of ocean waves in the local rest frame given by $\omega_0^2(k)=gk+\tau k^3$, where g(= 9.8 m/s^2) is the gravitational acceleration, and τ(= 7.4 × 10^{-5} m^3/s^2) is the ratio of the surface tension to the density of water. To a first order, Eq. (3) has a solution (Hughes, 1978; Alpers and Hennings, 1984)

$$N(\mathbf{k};\mathbf{r},t)=N_0(\mathbf{k})+\frac{\partial N_0(\mathbf{k})}{\partial\mathbf{k}}\frac{1}{\mu(\mathbf{k})}\mathbf{k}\cdot\frac{\partial\mathbf{U}(\mathbf{r},t)}{\partial\mathbf{r}}, \tag{4}$$

where N_0 is the action spectrum at equilibrium state, and $\mu(\mathbf{k})=0.04k^2u_*^2\Theta(\theta)/\omega(k)$ is the relaxation rate of the waves of wave vector $\mathbf{k}$ with u_* being the friction velocity given by (Amorocho and de Vries, 1980)

$$u_*=W\left(0.00104+\frac{0.0015}{1+\exp\left(-\left(W-12.5\right)/1.56\right)}\right)^{\frac{1}{2}}, \tag{5}$$

where W is the wind speed at 10 m height above sea surface, and $\Theta(\theta)=|\cos(\theta-\theta_W)|$ is the directional dependence of μ on the wind direction of angle θ_W of wind vector $\mathbf{W}$ and θ is the angle of $\mathbf{k}$. The action spectrum is related to the waveheight spectrum ψ by $N=(\omega_0/k)\psi$ and $N_0=(\omega_0/k)\psi_0$, where ψ_0 is the ambient waveheight spectrum. By substituting ψ and ψ_0 in Eq. (4), and differentiating in parts, the following equation can be obtained.

$$\psi(\mathbf{k})=\psi_0(\mathbf{k})+\left[\frac{\partial\psi_0(\mathbf{k})}{\partial\mathbf{k}}+\frac{\hat{\mathbf{k}}\psi_0(\mathbf{k})}{k}\left(\frac{c_g(k)}{c_p(k)}-1\right)\right]\frac{1}{\mu(\mathbf{k})}\mathbf{k}\cdot\frac{\partial\mathbf{U}(\mathbf{r},t)}{\partial\mathbf{r}}, \tag{6}$$

where $\hat{\mathbf{k}}$ is the unit vector of $\mathbf{k}$, $c_p(k)=\omega_0(k)/k$ is the wave phase velocity, and $c_g(k)=\partial\omega_0(\mathrm{k})/\partial k$ is the wave group velocity. This is the result of Alpers and Hennings (1984), and used by Holliday et al. (1986) for comparison between the Bragg and Kirchhoff scattering models. In order to advance further, the following Phillips spectrum is considered as the equilibrium wave height spectrum.

$$\psi_0(\mathbf{k})=\frac{6\times10^{-3}}{\pi}\Theta(\theta)k^{-4}\exp\left(-\frac{k_0}{k}\right), \tag{7}$$

where $k_0=g/W^2$. Eq. (6) then becomes

$$\frac{\psi(\mathbf{k},\mathbf{r})}{\psi_0(\mathbf{k})}=1+\frac{\hat{\mathbf{k}}}{k}\left(\frac{k_0}{k}+\frac{c_g(k)}{c_p(k)}-5\right)\frac{1}{\mu(\mathbf{k})}\mathbf{k}\cdot\frac{\partial\mathbf{U}(\mathbf{r},t)}{\partial\mathbf{r}}, \tag{8}$$

which is the general result for the waveheight spectrum perturbed by a slowly-varying current $\mathbf{U}$.

3. Varying Surface Current Induced by ISW: KdV Equation

An oceanic IW in a two-layer ocean can be described with a dimensional form of the KdV equation. From the KdV equation, the horizontal current velocity induced by ISW near the sea surface can be described as (Osborne and Burch, 1980; Zheng et al., 2001)

$$\mathbf{U}(\mathbf{r},t)=u_0\,\mathrm{sec\,h}^2\left[\frac{\mathbf{r}-Vt}{\Delta}\right], \tag{9}$$

where

$$u_0=c_0\eta_0/h_1 \tag{10}$$

is the peak current speed, η_0 is soliton amplitude,

$$c_0\cong\left(g\left(\rho_2-\rho_1\right)h_1h_2/\rho_2h_1+\rho_1h_2\right)^{\frac{1}{2}} \tag{11}$$

is the linear phase speed, h_1 and h_2 are the thickness of the upper and lower layers respectively, and ρ_1 and ρ_2 are the uniform water density of the upper and lower layers respectively. In Eq. (9), $V=c_0-(\alpha\eta_0/3)$ is the nonlinear soliton velocity and parameter $\Delta=(-12\gamma/\alpha\eta_0)^{\frac{1}{2}}$ is the characteristic half width, where γ and α are the dispersion and nonlinear coefficient respectively. γ and α read

$$\begin{aligned}\gamma&=\frac{c_0h_1h_2}{6}\frac{\rho_1h_1+\rho_2h_2}{\rho_2h_1+\rho_1h_2},\\ \alpha&=\frac{3}{2}\frac{c_0}{h_1h_2}\frac{\rho_2h_1^2-\rho_1h_2^2}{\rho_2h_1+\rho_1h_2},\end{aligned} \tag{12}$$

III. DATA AND METHOD

The proposed method is a combination of the KdV, ABE, and SPM to estimate the ISW amplitude. Detail algorithm flow is

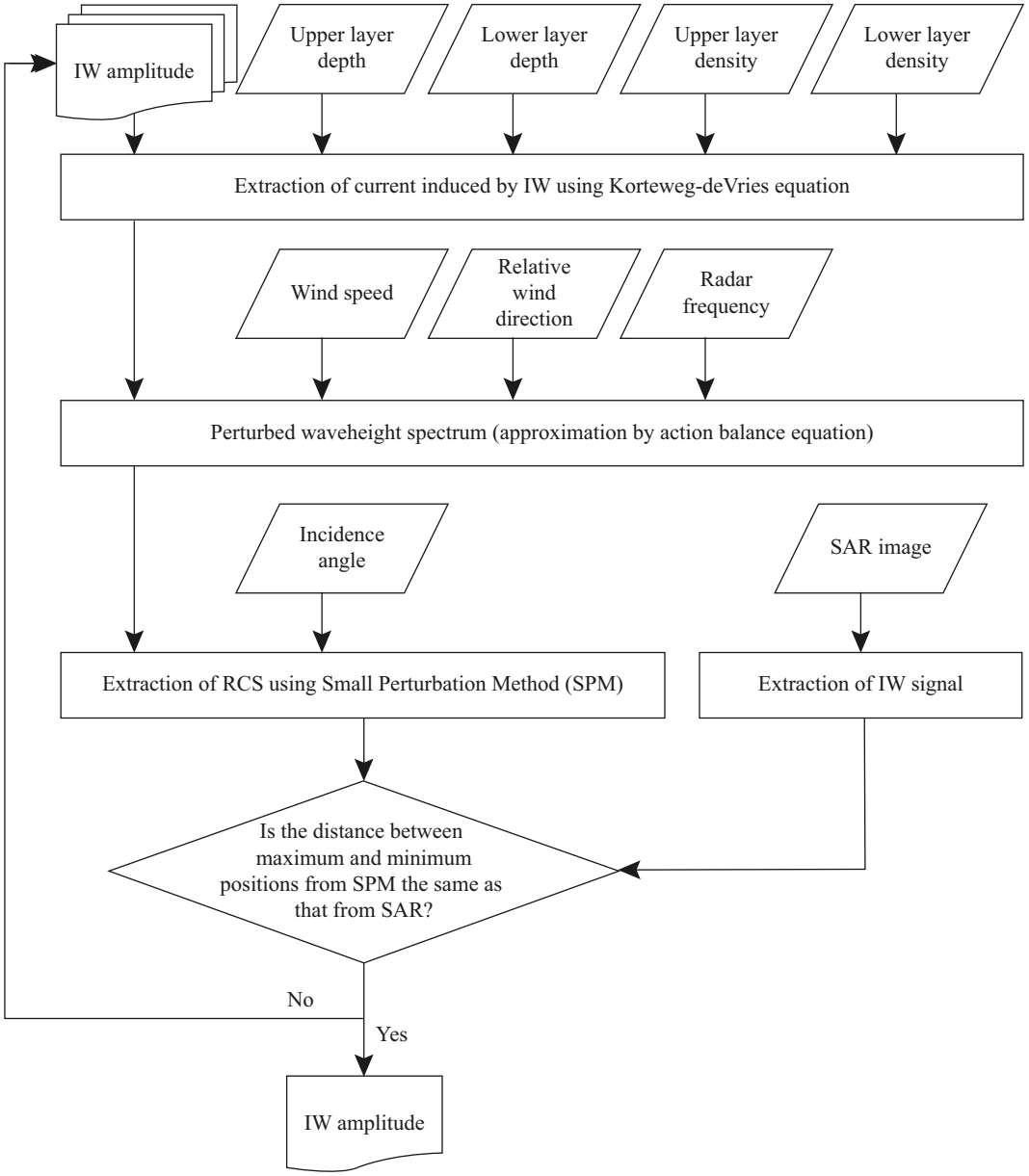

Fig. 1. Flow chart to estimate the IW amplitude.

presented in Fig. 1. In order to estimate the ISW amplitude, the information of water densities, pycnocline depth, water depth, wind speed, wind direction, radar frequency and incidence angle is needed. The SAR data used in this study were acquired by RADARSAT-1 SAR (Extended low beam mode) over the east coast of the Korean Peninsula at 21:37 (UTC) on the 5 of July 2000 as shown in Fig. 2. The frequency and polarization combination are 5.3 GHz (C-band) and HH-polarization respectively. In the SAR image, ISW used in this study appears to propagate northward from the Strait of Korea to Ulleung Basin. As we mentioned above, there are two different mechanisms for IW generation off the east coast of Korean Peninsula: those generated by wind-induced near-inertial wave (Kim et al., 2001; Kim et al., 2005) and those originated in internal tide (Lie et al., 1992; Park and Watts, 2006; Nam and Park, 2008; Jeon et al., 2014). In Fig. 2(b), we can faintly see the ISW group (around 36.8°N) that is presumed to have been generated earlier than the ISW of interest (black square box) in this paper. The distance between two ISW groups is approximately 63 km. If we assume that the ISW propagation speed is 1.5 m/s, the generation period of ISWs is 11.6 hours close to the semi-diurnal period (12.42 hours) rather than near-inertial period (~20 hours). It is also confirmed that those ISWs were generated by the spring tide in the Korea Strait. Fig. 3 shows the tidal elevation in the Korea Strait (longitude: 130.0°E, latitude: 36.6°N) from 20 June 2000 to 21 July 2000 obtained from the OSU Tidal Data Inversion (Egbert and Erofeeva, 2002). Since the ISWs are observed approximately 95 km off the Korea Strait before 17.6 hours from the SAR obser-

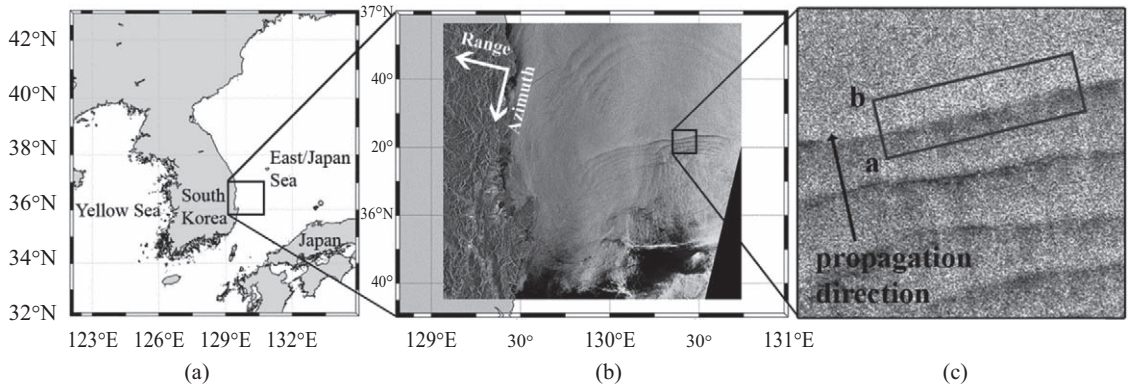

Fig. 2. Location of the experimental test site (a), RADARSAT-1 SAR image of ISWs over the east coast of the Korean Peninsula (b), and enlarged image (c). The ISW signature in the black box is used for analyses.

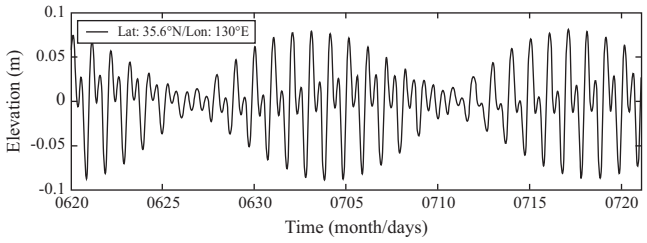

Fig. 3. Tidal elevations in Korea Strait (longitude: 130°E; latitude: 35.6°N) from 20 June 2000 to 21 July 2000.

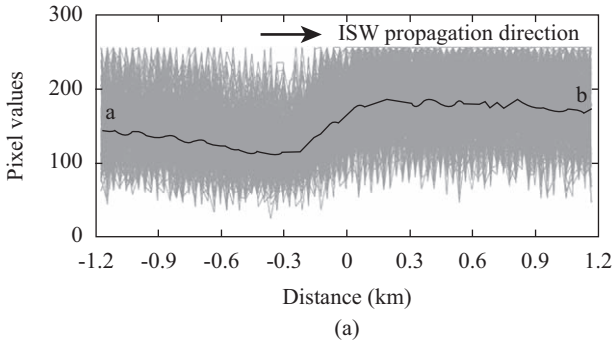

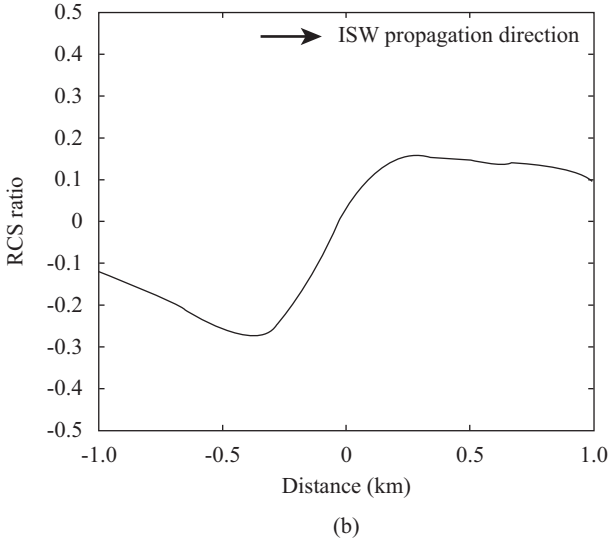

Fig. 4. Profiles of ISW in the propagation direction at ROI (a) and the representative RCS ratio of ISW (b).

vation time, it is certain that they were generated by the spring tide. Fig. 2(c) shows the SAR image of several ISW packets and there are bright areas in the front followed by dark areas in the direction of propagation. This is a typical feature of depression ISWs, where the upper layer or pycnocline depth (h_1) is smaller than the lower layer depth (h_2) in the stratified ocean (Liu et al., 1998). In the present study, the image modulation in the black rectangle area in Fig. 2(c) is examined for its strong modulation and straight feature of ISW signature. Front and rear 39 pixels (1,181.817 m) from the center of crest along the propagation direction are selected for the analyses with 30.3 m resolution. The individual pixel values along the propagation direction are shown in Fig. 4(a) as gray lines with their mean by a solid black line. For comparison with the RCS computed by the SPM, the mean pixel values are converted to the RCS, and normalized by the mean pixel values of ambient sea surface areas where ISWs are absent. The normalized and smoothed RCS by a moving window of 11 pixels is shown in Fig. 4(b).

Given the parameters of wind and ocean, the backscatter RCS can be calculated and compared with the SAR image. There are several other unknown parameters that need to be assumed or provided from external sources. In the following, water temperature and the densities (ρ_1 and ρ_2) by the Hybrid Coordinate Ocean Model (HYCOM) data based on the Navy Coupled Ocean Data Assimilation (NCODA) system for data assimilation are utilized in order to simulate the ISW using the KdV equation. Fig. 5(a) shows the profiles of water temperature, density and buoyancy frequency (longitude: 130.5°E; latitude: 36.3°N) obtained from HYCOM. It can be seen that the temperature is steadily decreased up to the water depth of 200 m with the increasing water density. The buoyancy frequency is the maximum at the water depth of 16 m. We cannot exactly define the upper layer depth since the temperature profile in Fig. 5(a) shows

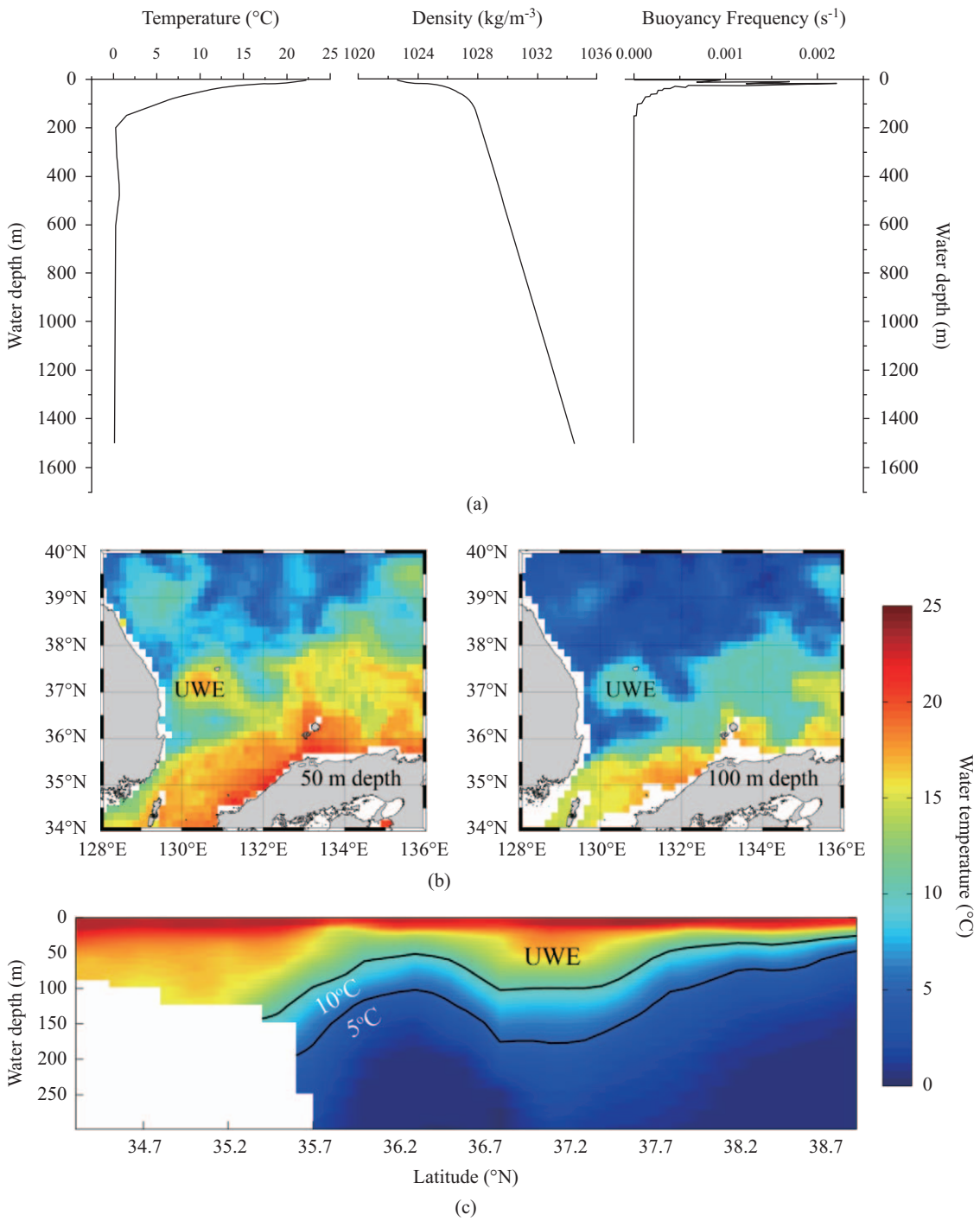

Fig. 5. Profiles of water temperature, density and buoyancy frequency (longitude: 130.5°E; latitude: 36.3°N) (a), the distributions of water temperature at 50 m and 100 m depths (b), and the vertical distribution of water temperature from 34.3°N to 38.9°N at longitude of 130.5°E (c). The solid contour represents 5°C and 10°C isotherms.

the stratified ocean structure that is typical in summer season. Park and Watts (2006) and Jeon et al. (2014) used the 5°C isotherm as a boundary for the surface and intermediate waters in East/Japan Sea, and Kim et al. (2001) examined the amplitude of ISWs using the 10°C isotherm. In this study, the 5°C and 10°C isotherms were examined for a boundary of upper and lower layers. Fig. 5(b) describes the distributions of water temperature at 50 m and 100 m depths, showing that Ulleung Warm Eddy (UWE) is isolated at around 37.0°N, 130.5°E, and relatively cold water is existed in the southern Korea Strait. Fig. 5(c) is the vertical distribution of water temperature from 34.3°N to 38.9°N at longitude of 130.5°E, and the solid contours represent

Table 1. The summary of input parameters.

Input parameters [units]	Values
Water depth [m]	1800
Upper layer depth [m]	52/102
Density of upper layer [kg m^{-3}]	1024.90/1026.02
Density of lower layer [kg m^{-3}]	1028.06/1028.26
Wind speed [m s^{-1}]	2.3
Relative wind direction [°]	9

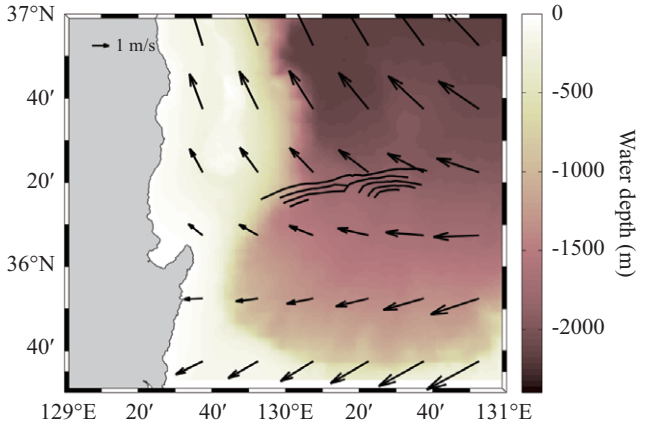

Fig. 6. The wind directions, water depth, and ISW crest lines at the SAR observation time. The arrows represents wind vector that superimposed on the water depth field.

5°C and 10°C isotherms. This figure shows the 5°C and 10°C isotherms are moved upward at around 36.3°N due to the isolation of UWE and inflow of cold water from the east coast of Korea. The upper layer depths (h_1) estimated by depths of 5°C and 10°C were 102 m and 52 m respectively at 36.3°N, 130.5°E.

Ocean wind data with a resolution of 0.25° was obtained from the cross-calibrated multi-platform ocean surface wind vector data derived under the Cross-Calibrated Multi-Platform (CCMP) project and contain a value-added 6-hourly gridded analysis of ocean surface winds (Atlas et al., 2011), and the water depth($h = h_1 + h_2$) with a high resolution of 0.0083° was acquired from the General Bathymetric Chart of the Ocean (GEBCO, http://www.gebco.net/). Fig. 6 shows the wind directions, water depth, and ISW crest lines at the SAR observation time. By interpolating the time of wind vectors, they were obtained to the same as the SAR observation time. Near the ISWs (longitude: 130.4°E; latitude: 36.4°N), the wind speed and relative wind direction to range direction were 2.3 m s^{-1} and 9° respectively. The water depth near the first crest of ISW (longitude of 130.5°E; latitude of 36.3°N) is 1,800 m. Table 1 shows the summary of input parameters obtained from above data and used for computing RCS.

There are two methods to compare the RCS values computed by the SPM and extracted from the SAR image. The first is the comparison of maximum and minimum values, and the second is the comparison of the distances between maximum and minimum (or peak and trough) positions ($d_{\text{min-max}}$). The first method is not possible since the magnitude of the C-band RCS ratio computed by the SPM is much smaller than that of SAR images. This is a characteristic of the SPM model at X-band and C-band while the model yields better and larger modulation at L-band. Nevertheless, the overall shapes and positions of peaks and troughs of the RCS modulation by the SPM are in agreement with those of SAR data (Amorocho and de Vries, 1980; Thompson and Gasparovic, 1986; Holliday et al., 1987; Ouchi et al., 1997). The ISW amplitude can be determined by matching the $d_{\text{min-max}}$ computed by the SPM to those by the SAR image. From the RCS ratio by the SAR image as shown in Fig. 4(b), the $d_{\text{min-max}}$ was computed as 666.7 m along the ISW propagation direction.

Although the $d_{\text{min-max}}$ has been used to understand the properties of the IWs by several researchers (Zheng et al., 2001; Chen et al., 2011; Xue et al., 2013), the suitability of the $d_{\text{min-max}}$ to figure out ISW amplitude in this model should be examined. Fig. 7 shows the RCS variations for different polarizations, incidence angles, radar frequencies, wind direction and wind speed with fixed current variations. Except the polarizations, all results represent the RCS ratio. The RCS modulated by ISW can be computed through a series of these procedures, and the RCS ratio is defined as

$$\frac{\delta\sigma(\mathbf{r})}{\sigma_0} = \frac{\delta\psi(k_B, \mathbf{r}) + \delta\psi(-k_B, \mathbf{r})}{\psi_0(k_B) + \psi_0(-k_B)}, \tag{13}$$

where $\delta\sigma(\mathbf{r}) = \sigma(\mathbf{r}) - \sigma_0$ is the RCS in the presence of a surface

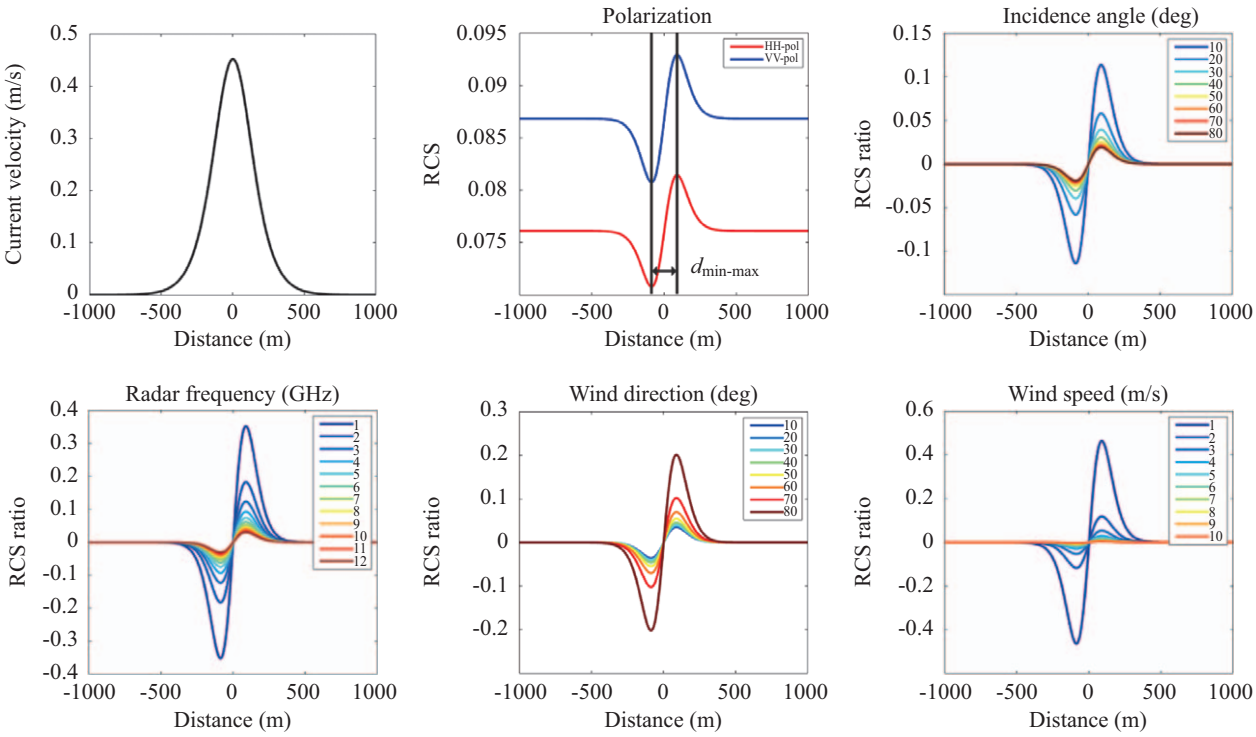

Fig. 7. The suitability confirmation of the dmin-max to figure out ISW amplitude. The figures show the RCS variations according to the change of polarizations, incidence angles, radar frequencies, wind direction and wind speed with fixed current variations.

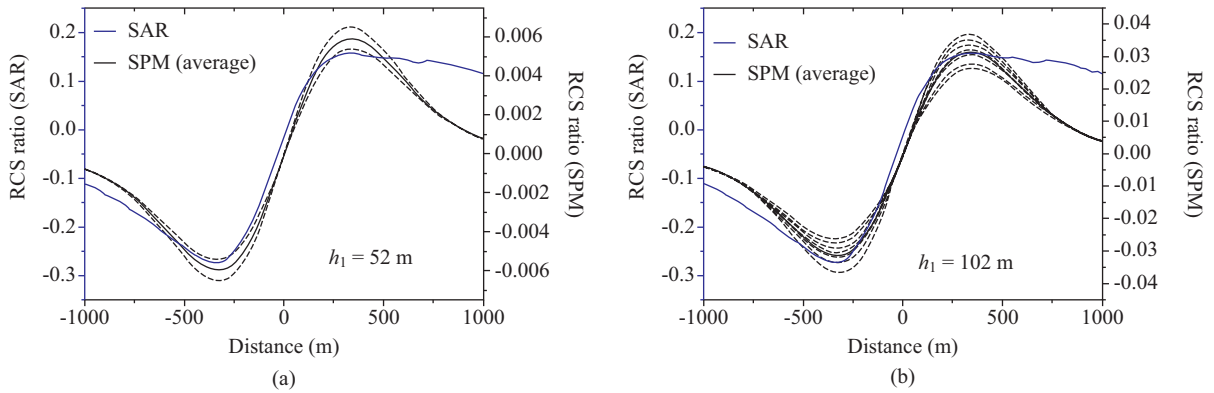

Fig. 8. The RCS ratios measured from the SAR image (blue solid lines) and computed by the SPM (black lines). The black broken lines and solid line are all results satisfying that the dmin-max by the SPM is the same as those by the SAR and black solid line represents average value respectively. The pycnocline depth h1 is assumed as 52 m (a) and 102 m (b).

current, and σ_0 is the RCS from the ambient sea surface. It shows that the increase of both incidence angle and radar frequency makes the decrease in the magnitude of RCS. In case of wind parameters, the increase of wind direction and wind speed causes the increase and decrease in the magnitude of RCS respectively. Note that the wind direction exactingly represents the angle between the wind and range directions. As can be seen, these parameters only affect the magnitude of RCS, but not the $d_{\text{min-max}}$. Thus, the ISW amplitude can be determined using the $d_{\text{min-max}}$.

IV. EXPERIMENTAL RESULTS AND DISCUSSIONS

Figs. 8(a) and (b) show the RCS ratio measured from the SAR image (blue solid line) and SPM (black lines) for h_1 = 52 m and h_1 = 102 m respectively. The black broken lines are the results satisfying the same $d_{\text{min-max}}$ of the SPM and the SAR image, and black solid line represents the average value of the black broken lines. As shown in Fig. 8, the overall shapes and positions of peaks and troughs of the RCS modulation by the

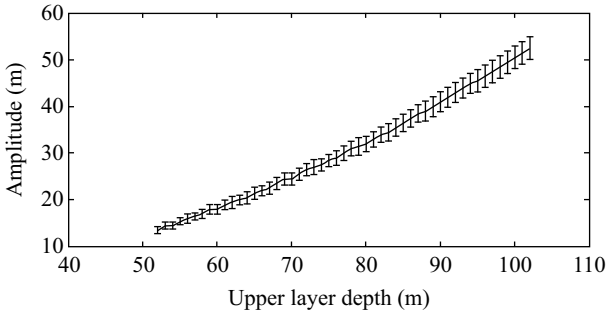

Fig. 9. ISW amplitudes in terms of upper layer depths ranging from 52 m to 102 m with 1 m intervals. The error bars represent the standard deviations.

SPM are in good agreement with those by the SAR image. The mean ISW amplitudes were extracted as 13.5 m and 52.5 m for h_1 = 52 m and h_1 = 102 m respectively. There are large differences of the ISW amplitude between the two upper layer depths. Thus, the relation between the ISW amplitude and the upper layer depth was examined. Fig. 9 shows the estimated ISW amplitudes for various upper layer depths ranging from 52 m to 102 m with the error bars representing the standard deviations. It shows that the amplitudes and the error scales increase with the increasing upper layer depth. The amplitude changes by 0.5 m~1.0 m as the upper layer depth varies every 1 m. It can be seen that the ISW amplitudes are very sensitive to the upper layer depth.

Although there are no simultaneous *in-situ* data to validate the results, the estimated amplitudes were in the appropriate range as compared to the previous studies. It represents that it is possible to derive the ISW amplitude if the upper layer depth can be known in stratified water columns. Among the previous studies, Jeon et al. (2014) observed the largest internal tide with the maximum displacement of 5°C isotherm reached up to 70 m in East/Japan Sea, and it refers that the maximum ISW amplitude was approximately 35 m by using the assumption that the amplitude is the half of the vertical displacement. With the maximum amplitude of 35 m, it can be also known that the upper layer depth might be less than 85 m since our observation area is far away from the continental shelf-slope region. Although the 5°C isotherm has been used as a boundary for the surface and intermediate waters in East/Japan Sea, in the summer time the line could be changed and an interaction between internal tides and ISWs is almost unknown.

V. CONCLUSIONS

In this paper, an approach is presented to estimating the amplitude of ISW from SAR data. The method is to compute the RCS from the waveheight spectrum in the presence of varying surface currents induced by ISW, and to compare the RCS ratio with that of the SAR image modulation. The SPM is used to compute the RCS, the wave-current interaction is described by the ABE, and the approximate solution of the KdV equation is used to describe the soliton and ISW amplitude. With this method, the average amplitudes of ISW in different upper layer depths were estimated using the RADARSAT-1 SAR data over the eastern waters of the Korean Peninsula for the first time. There is no *in-situ* data at the time of SAR data acquisition to validate the results, and further rigorous study is required to test the theory using simultaneous *in-situ* measurements with SAR data. Such experiments require careful planning, organization and pre-preparation. We have shown in this paper that our results are well within the previous measurements, and are the first of its kind to initiate such future planned experiments in the waters where the properties of ISWs are hitherto little known. Thus, despite the need for further rigorous validation, the method based on the SPM and KdV equation for ISW amplitude retrieval described in the present paper appears as a promising tool as illustrated by the example using RADARSAT-2 data in the waters around Korean peninsula.

ACKNOWLEDGEMENTS

This research was a part of the projects entitled “Development of Ship-handling and Passenger Evacuation Support System”, “Construction of Ocean Research Stations and their application Studies, Phase 2”, “Base Research for Building Wide Integrated Surveillance System of Marine Territory”, and “Development of Korea Operational Oceanographic System (KOOS), Phase 2” funded by the Ministry of Oceans and Fisheries, Korea.

REFERENCES

Alford, M. H. (2003). Redistribution of energy available for ocean mixing by long-range propagation of internal waves. Nature 423, 159-162.

Alpers, W. and I. Hennings (1984). A theory of imaging mechanism of underwater bottom topography by real and synthetic aperture radar. Journal of Geophysical Research 89(C6), 10529-10546.

Amorocho, J. and J. J. de Vries (1980). A new evaluation of wind stress coefficient over water surfaces. Journal of Geophysical Research 85(C3), 413-422.

Apel, J. R. (2002). An atlas of oceanic internal solitary waves: oceanic internal waves and solitons. In: Global Ocean Associates, VA, USA.

Atlas, R., R. N. Hoffman, J. Ardizzone, S. M. Leidner, J. C. Jusem, D. K. Smith and D. Gombos (2011). A cross-calibrated, multiplatform ocean surface wind velocity product for meteorological and oceanographic applications. Bulletin of the American Meteorological Society 92, 157-174.

Chen, G.-Y., F.-C. Su, C.-M. Wang, C.-T. Liu and R.-S. Tseng (2011). Derivation of internal solitary wave amplitude in the South China Sea deep basin from satellite images. Journal of Oceanography 67(6), 689-697.

Chen, G. Y., C. T. Liu, Y. H. Wang and M. K. Hsu (2011). Interaction and generation of long-crested internal solitary waves in the South China Sea. Journal of Geophysical Research: Oceans 116, C06013.

Demir, M. A., J. T. Johnson and T. J. Zajdel (2012). A study of the fourth-order small perturbation method for scattering from two-layer rough surfaces. IEEE Transaction on Geoscience and Remote Sensing 50(90), 3374-3382.

Ding, Y. and S. S. Wang (2011). Modeling of wave-current interaction using a multidirectional wave-action balance equation. Coastal Engineering Proceedings 1(32), 47.

Egbert, G. and S. Erofeeva (2002). Efficient Inverse Modeling of Barotropic Ocean Tides. Journal of Atmospheric and Oceanic technology 19, 183-204.

Holliday, D., G. St-Cyr and N. E. Woods (1986). A radar ocean imaging model for small to moderate incidence angles. International Journal of Remote Sensing 7(12), 1809-1834.

Holliday, D., G. St-Cyr and N. E. Woods (1987). Comparison of a new radar ocean imaging model with SARSEX internal wave image data. International Journal of Remote Sensing 8(9), 1423-1430.

Hughes, B. A. (1978). The effect of internal waves on surface wind waves: Part 2, theoretical analysis. Journal of Geophysical Research 83(C1), 455-465.

Hyder, P., D. R. G. Jeans, E. Cauquil and R. Nerzic (2005). Observations and predictability of internal solitons in the Northern Andaman Sea. Applied Ocean Research 27, 1-11.

Jackson, C. R. (2004). An atlas of internal solitary-like waves and their properties. In: Global Ocean Associates, VA, USA.

Jackson, C. R., J. C. B. da Silva and G. Jeans (2012). The generation of nonlinear internal waves. Oceanography 25(2), 108-123.

Jeon, C., J.-H. Park, S. M. Varlamov, J.-H. Yoon, Y. H. Kim, S. Seo, Y.-G. Park, H. S. Min, J. H. Lee and C.-H. Kim (2014). Seasonal variation of semidiurnal internal tides in the East/Japan Sea. Journal of Geophysical Research 119, 2843-2859.

Kim, D.-J., S. H. Nam, H. R. Kim, W. M. Moon and K. Kim (2005). Can near-inertial internal waves in the East Sea be observed by synthetic aperture radar?. Geophysical Research Letters 32(2), L02606.

Kim, H.-J., Y.-G. Park and K. Kim (2005). Generation mechanism of near-inertial internal waves observed off the East Coast of Korea. Continental Shelf Research 25, 1712-1719.

Kim, H. R., S. Ahn and K. Kim (2001). Observations of highly nonlinear internal solitons generated by near-inertial internal waves off the east coast of Korea. Geophysical Research Letters 28(16), 3191-3194.

Klein, L. A. and C. T. Swift (1977). An improved model for the dielectric constant of sea water at microwave frequencies. IEEE Transactions on Antennas and Propagation AP-25, 104-111.

Korteweg, D. J. and G. De Vries (1895). On the change of form of long waves advancing in a rectangular canal, and on a new type of long stationary waves. Philosophical Magazine 39(240), 422-443.

Lamy, M., J. M. Le Caillec, R. Garello and A. Kenchaf (2004). Short wave spectrum modulation by a surface current field and long waves for SAR imaging process simulation. Geoscience and Remote Sensing Symposium, IGARSS'04 Proceedings 5, 3100-3102.

Li, D., X. Chen and A. Liu (2011). On the generation and evolution of internal solitary waves in the northwestern South China Sea. Ocean Modelling 40, 105-119.

Lie, H. J., C. W. Shin and Y. H. Seung (1992). Internal tidal oscillations of temperature off Jukbyun on the east coast of Korea. Journal of the Korean Society of Oceanography 27(3), 228-236. (in Korean)

Liu, A. K., Y. S. Chang, M.-K. Hsu and N. K. Liang (1998). Evolution of nonlinear internal waves in the East and South China Sea. Journal of Geophysical Research 104(C4), 7995-8008.

Lyzenga, D. R., G. O. Marmorino and J. A. Johannsessen (2004). Ocean currents and current gradients. In: Jackson CR. et al. (ed) Synthetic Aperture Radar, Marine User's manual, 207-220.

Moreira, A., P. Prats-Iraola, Y. Younis, K. Krieger, I. Hajnsek and K. P. Papathanassios (2013). A tutorial on synthetic aperture radar. IEEE Geoscience and Remote Sensing Magazine 1(1), 6-43.

Muacho, M., J. C. B. da Silva, V. Brotas and P. B. Oliveira (2013). Effect of internal waves on near-surface chlorophyll concentration and primary production in the Nazare Canyon (west of the Iberian Peninsula). Deep-Sea Research 81, 89-96.

Nam, S. H. and J.-H. Park (2008). Semidiurnal internal tides off the east coast of Korea inferred from synthetic aperture radar images. Geophysical Research Letters 35(5), L05602.

Nycander, J. (2005). Generation of internal waves in the deep ocean by tides. Journal of Geophysical Research 110(C1), 1-9.

Osborne, A. R. and T. L. Burch (1980). Internal solitons in the Andaman Sea. Science 208(4443), 451-460.

Ouchi, K., N. R. Stapleton and B. C. Barber (1997). Multi-frequency SAR images of ship-generated internal waves. International Journal of Remote Sensing 18(18), 3709-3718.

Park, J.-H. and R. Watts (2006). Internal tides in the Southwestern Japan/East Sea. Journal Physical Oceanography 36, 22-34.

Pormar, L., M. Morsilli, P. Hallock and B. Bádenas (2012). Internal waves, an under-explored source of turbulence in the sedimentary record. Earth-Science Reviews 111, 56-81.

Rice, S. O. (1951). Reflection of electromagnetic waves from slightly rough surface. Communications on Pure and Applied Mathematics 4, 351-378.

Thompson, D. R. and R. F. Gasparovic (1986). Intensity modulation in SAR images of internal waves. Nature 320, 345-348.

Ulaby, F. T., R. K. Moore and A. K. Fung (1982). Microwave remote sensing: active and passive. Addison –Wesley, Reading, MA, USA, 816-842, 853-860.

Valenzuela, G. R. (1968). Scattering of electromagnetic waves from a tilted slightly rough surface. Radio Science 3, 1057-1066.

Wright, J. W. (1968). A new model for sea clutter. IEEE Transactions on Antennas and Propagation AP-16(2), 217-223.

Xue, J., H. C. Graber, B. Lund and R. Romeiser (2013). Amplitudes estimation of large internal solitary waves in the Mid-Atlantic Bight using synthetic aperture radar and marine X-band radar images. IEEE Transactions on Geoscience and Remote Sensing 51(6), 3250-3258.

Yang, J., J. Zhang and J. Meng (2010). Underwater topography detection of Taiwan Shoal with SAR images. Chinese Journal of Oceanology and Limnology 28(3), 636-642.

Zheng, Q., Y. Yuan, V. Klemas and X.-H. Yan (2001). Theoretical expression for an ocean internal soliton synthetic aperture radar image and determination of the soliton characteristic half width. Journal of Geophysical Research 106(C11), 31415-31423.

Zhou, J. X. and X.-Z. Zhang (1991). Resonant interaction of sound wave with internal solitons in the coastal zone. The Journal of the Acoustical Society of America 90(4), 2042-2054.